83. Algorithm for enabling monitoring of plant water deficit by a low-cost thermal IR camera

N. Oz [1,3], O. Berman [1,3], N. Sochen [2], D. Mendlovic [3] and I. Klapp[1,*]
[1]*Department of Sensing, Information and Mechanization Engineering, ARO- Volcani Institute, Bet Dagan, Israel; * iftach@volcani.agri.gov.il*
[2]*Department of Applied Mathematics, Tel Aviv University, Tel Aviv 69978, Israel*
[3]*School of Electrical Engineering, Tel-Aviv University, Tel-Aviv, Israel*

Abstract

Plant temperature is a key indicator of plant health, particularly for detecting water stress. While radiometric thermal IR cameras can detect such stress early, their high-cost limits widespread agricultural use. Low-cost uncooled thermal cameras offer potential but face challenges, including drift, non-uniformity, low accuracy (approx. ±5°C), and limited spatial resolution. This study addresses these issues by developing end-to-end deep-learning methods for non-uniformity correction and super-resolution. Results of the proposed method demonstrated real-time processing of raw low-cost thermal IR camera data, showing high fidelity, with a small root mean square error of approx. 0.5°C relative to a scientific-graded radiometric camera. The crop water stress index derived from the processed data showed minimal deviation (approx. 1.4–1.9%) from scientific-grade results.

Keywords: crop water stress index, machine learning, super-resolution, uniformity correction

Introduction

Plant temperature is a central indicator of plant health and a main target in the agricultural monitoring process of the open field (Mahlein., 2016; Das *et al*., 2020). To protect the plant from dehydration, in the presence of a water deficit, many plant species close the stoma of the leaf, resulting in a rise in canopy temperature. Previous work has shown that radiometric thermal IR (long wave infrared) cameras can detect irrigation deficits related to this mechanism long before it is noticed in the visible domain. The change in the canopy temperature due to water stress is expressed by rising only a few degrees centigrade. Thus, the thermal camera for agricultural monitoring requires very high accuracy in the order of one-degree centigrade.
The development of drone technology enables these cameras to monitor the whole field. However, while this technology is essential for water management, its implementation has been minimal, mainly due to the high cost of radiometric thermal IR cameras (20000$ and more).
Developments in micro-bolometer technology have allowed the development of low-cost uncooled thermal cameras for approx. US$4000 or less. While this technology is promising, it suffers from a few main drawbacks: drift and non-uniformity in temperature measurement and too low-temperature accuracy of typically five degrees centigrade. In addition, the thermal cameras are characterized by a small detector array of quarter video graphics array (QVGA) and video graphics array (VGA), resulting in a small resolution that limits the flying altitude.
This work presents progress in closing these gaps to enable low-cost IR thermal cameras for agricultural monitoring needs. The objectives were to develop a two-stage algorithmic method to mitigate the non-uniformity and improve the spatial resolution. The aim was to demonstrating the proposed method on raw data from a low-cost camera and compare the results to the measurements of a scientific camera.

Materials and methods

Single image non-uniformity correction
Typically, the pixel response in a low-cost, uncooled thermal IR camera is not uniform, i.e., every pixel has a different gain and offset. The camera is uncooled and thus emits thermal radiation, some of it on the detector, (self-radiation), which results in drift in the non-uniform response. The linear model for the resulting image formation is shown in Eq. 1 (Klapp *et al.*, 2017):

$$r[k,l;T_{\text{amb}},T_{\text{obj}}[k,l]] = g[k,l;T_{\text{amb}}] \cdot s[k,l;T_{\text{obj}}] + o[k,l;T_{\text{obj}}] + n[k,l] \quad (1)$$

The grey level reading associated with the object temperature is denoted as r, the gain is denoted by g, the offset is denoted by o, the raw reading is denoted by s, and the noise is denoted by n. The pixel coordinates are marked (k,l), the ambient temperature is marked with T_{amb}, and the object's temperature is marked with T_{obj}.

Figure 1 illustrates a low-cost camera image formation section from object point (x*). The influence of the ambient temperature on the camera readings tied to the self-radiation originates from the uncooled envelope of the camera (d*) which, added to the measured radiation field on the detectors array (detector), propagates from point (x*)

Calibration setup and camera model
Supervised training requires pairs of perfectly aligned degraded and ground truth images. With a large enough dataset, one can train a convolutional neural network with the degraded image and ambient temperature as an input and the ground truth as a target for the output. It is unrealistic to have perfectly aligned pairs; any inconsistent shift or projection between the two images confuses the trained model and results in an error. Using a series of images of a black body taken by the low-cost camera placed in an environmental chamber allows mapping of the camera response (Nugent *et al.*, 2013). Using this dataset, a model of the low-cost camera as a function of object temperature map and ambient temperature has been suggested (Oz *et al.*, 2024a). Using this model, a series of aligned images were generated in response to a series of inputs measured by a scientific-graded radiometric camera, FLIR A655Sc, Teledyne FLIR (Wilsonville, OR, USA). The resulting pairs were

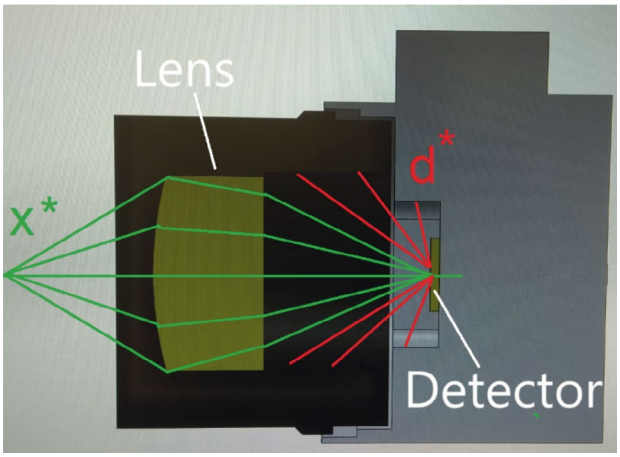

Figure 1. Image formation in a low-cost, uncooled thermal camera.

used to train a non-uniformity correction model. $R[k,l;T_{amb},T_{obj}[k,l]]$ mimics the camera response of the low-cost camera. A simplified form of the model is given in Eq. 2:

$$R[k,l;T_{amb},T_{obj}[k,l]] = \left\{\sum_{m=0}^{M_{rad}}\left(\sum_{n=0}^{M_{poly}} B(n,T_{amb})\cdot[P]^m\right)\cdot[k,l]\right\}\cdot\left(T_{obj}[k,l]\right)^m \quad (2)$$

where (T_{obj}) is the temperature of the object, (k,l) are the spatial coordinates of the image, M_{rad} is the number of coefficients in the radial fit, M_{poly} is the order of the polynomial fit, and [P] is a radial kernel matrix. $B(n,T_{amb})$ is the radial dependent function derived from the radial fitting of the black body measurements in various objects and ambient temperatures.

Thermal image non-uniformity correction (NUC)

Following the above, it is assumed that a NUC can be treated as a regression between a series of corrupted and ground truth data. In recent work, given a grey level input of a thermal camera, Oz *et al.* (2024a) suggested a method to consider the correction of the spatial uniformity as well as the temperature of the object. The proposed CNN algorithm relies on a U-NET backbone (Ronneberger *et al.*, 2015), using the ambient temperature as a secondary input. In addition, it has been shown that including the physical model of the system Eq.(1) improves the restoration accuracy. Figure 2. presents experimental results (Oz *et al.*, 2024b). The grey shaded background is the ground truth image taken by the FLIR A655Sc, radiometric camera, in color temperature differences between the estimated temperature from the low-cost raw image to the ground truth. The field of view of the low-cost camera is smaller. The mean absolute error (MAE) is 0.44°C, where most of the error appears against the sky, probably due to slight motion during the integration time. A more accurate model with a series of images as input is demonstrated in Oz *et al.* (2024b). results of this model in an end-to-end pipeline can be found in Oz *et al.* (2025).

Single image super-resolution

The native size of a low-cost thermal infrared image is small, typically between QVGA (240×320) and VGA (480×640). Small spatial resolution limits the minimum resolved detail. This becomes critical

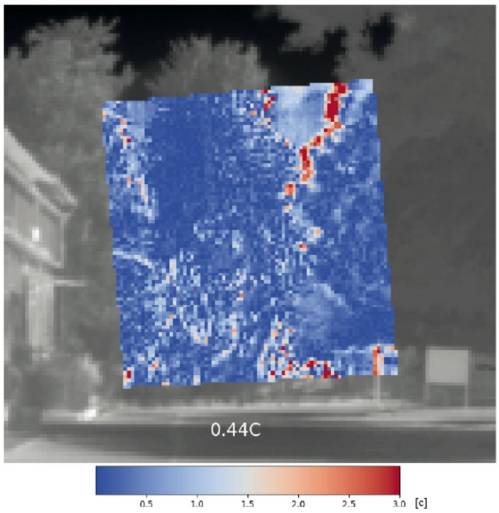

Figure 2. Example for NUC and temperature estimation (Adapted from Oz *et al.*, 2024b).

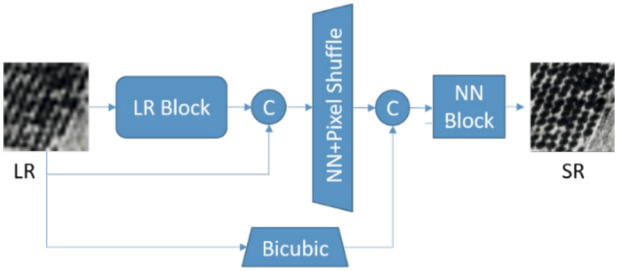

Figure 3. CNN-based SR schema.

in remote sensing, where minimum flight height is dictated by regulations or minimal coverage of the field of view. In thermal imagery, with an increase in altitude, adjunct objects such as ground and crops in a raw crop can mix, resulting in mixed pixels and false temperature estimation. To improve the spatial resolution of the image, it is suggested that a high-resolution image be estimated by a super-resolution (SR) algorithm right after the non-uniformity is corrected for the native image.

Single-image SR is very attractive due to the minimal required input. Various single-image algorithms have been suggested previously, which typically rely on large convolutional neural networks, which require large datasets for training and high computational power to support the SR process. The most notable for this use is the very deep super resolution (VDSR) (Kim *et al.*, 2016). With agricultural needs in mind, in previous work, Oz *et al.* (2020) suggested a single image SR CNN scheme relying on low computational power (Figure 3). The proposed system is based on an unbalanced U-Net-like neural network. To save computation, most processing is performed in a low-resolution domain. The many channels from the low-resolution (LR) block are concatenated (denoted C) into a block composed of a few CNN layers. A pixel shuffle block then upscales the image to the required super-resolution ×2 or ×4 dimension. Finally, the outcome of the channel is added and processed together with a bicubic interpolation of the input; that is, the algorithm is trained to learn complementary information beyond what can be easily gained by bicubic interpolation. The low-resolution input is denoted LR, while the super-resolution image is denoted SR.
Typical results of the SR, presented in Figure 4, show that Oz *et al.* (2020) aligned with the state-of-the-art single image method, such as VDSR. Compared to the VDSR, the proposed method used only 3% computation power.

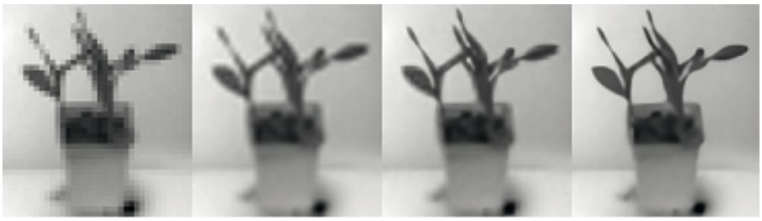

Figure 4. Example for super-resolution process (Adapted from Oz *et al.*, 2020). (a) LR input image. (b) Bicubic interpolation by a factor of ×4. (c) Results of the VDSR algorithm. (d) Results of the SR algorithm proposed by Oz *et al.* (2020).

End-to-end pipeline

The proposed pipeline follows the previously suggested pipeline (Klapp *et al*. 2021); the replacement of the NUC stage with a machine learning algorithm written in convolutional neural network architecture allows for the smooth merging of the NUC block with the SR block. In addition, the compact implementation of the blocks allows for the real-time implementation and demonstration of real-world data. The pipeline gets raw measurements of the thermal camera as an input where the output of the system is ×2 or ×4 temperature map.

Crop water stress index (CWSI)

Plant water status is indicated by the ratio of the difference between plant temperature (T_{plant}) and the temperature of a well-hydrated plant ($T_{\text{plant}}-T_{\text{wet}}$), to the difference between plant temperature and a severely stressed plant ($T_{\text{plant}}-T_{\text{dry}}$) (Katz *et al*., 2022). This ratio, known as the crop water stress index (CWSI), is given in Eq. 3:

$$\text{CWSI} = \frac{T_{\text{plant}}-T_{\text{wet}}}{T_{\text{plant}}-T_{\text{dry}}} \tag{3}$$

As the plant temperature gets closer to T_{wet}, the availability of water improves. In contrast, approaching T_{dry} reflects a stressed plant. Previous work has shown that CWSI can be directed and estimated using thermal radiometric imagery (Bahat *et al*., 2021; Berni *et al*., 2009).

Dataset for CWSI estimation

Experiments were conducted at four agricultural sites in Israel – Sede Nehamia, Gevim, Sede David, and Mevo Bytar – on various crops, including almonds, avocados, citrus and jojoba. One aerial image per crop field was analyzed, except for grapes, where two aerial images per field were analyzed. The study was conducted over three growing seasons: 2021, 2022 and 2023. Measurements were taken with a FLIR A655Sc radiometric camera. These images were used to simulate images of the low-cost raw data of the thermal camera, FLIR TAU2, Teledyne FLIR (Wilsonville, OR, USA). The generation of the low-cost images is done using the generator presented in Eq. (2). Where T_{obj}[k,l] was the image of the FLIR A655Sc radiometric camera. The generator output $R[k,l;T_{\text{amb}},T_{\text{obj}}[k,l]$, was the simulated images of the low-cost FLIR TAU2 thermal camera to the same scenes. The camera model was calibrated in the lab using FLIR TAU2 images of a blackbody in various (T_{amb},T_{obj}) combinations as in Oz *et al.* (2024a).

Side-by-side experimental setup

The proposed pipeline was tested on 46 pairs of real data collected in the field (Oz *et al*., 2024b). The experimental setup comprised two cameras, FLIR A655Sc. In Figure 5, the cameras are bordered by yellow frames and marked with the letters A and B, respectively. The two cameras were triggered simultaneously through a Raspberry PI microcomputer. The experiment was done on a clear day in July 2023 in a field at Volcani Institute, Israel. The experimental setup relied on two camera arrangements, low-cost and scientific, imaging simultaneously carried by the same drone. The FLIR TAU2 camera provided low-cost images, and the images were collected when all factory settings were disabled, and only a single-point correction was made before the drone took off. Following the flight, the collected raw data was processed using the proposed end-to-end method and compared to temperature maps taken by the FLIR A655Sc scientific camera; the processing time of the raw low-cost data took less than a second per frame.

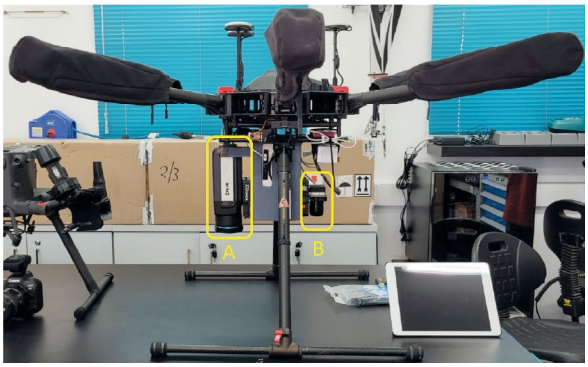

Figure 5. Side-by-side experimental setup. Adapted from Oz *et al.* (2024b).

Results and discussion

Single image super-resolution and non-uniformity correction in video rate
Two real-world experimental examples of the pipeline are presented in Figure 6. The grey background is the temperature map measured by the FLIR A655Sc camera. Fig.6a is the results of the proposed pipeline using SR ×2, while Figure 6b is the results of the proposed pipeline using SR×4. The field of view of the low-cost camera is smaller. The temperature errors between the pipelines are relative to the ground truth in the overlapping area presented in the coloured rectangle. The mean absolute error (MAE) is 0.87 and 1.08°C, respectively. For more results, see Oz *et al.* (2025).

CWSI calculations
The FLIR A655Sc was used to calculate the ground truth CWSI values and generate degraded raw grey level images mimicking FLIR TAU2 images of the same scene. The confidence in the generator model (Eq. 2) comes from very good results in using the same generator to create the dataset for training the NUC models (Oz *et al.*, 2024b, 2025) and the success of these trained models in restoring with only small error the scene temperature from raw data measured by the FLIR TAU2 camera.
The CWSI calculations were done for both processed images of the generated FLIR TAU 2 measurements performed by the proposed pipeline and those taken by the FLIR A655Sc camera. Experimental results show that the processed data was in excellent fidelity to the temperature map measured by the scientific camera. The root mean square error was approx. 0.5 centigrade. Comparing the calculations results of CWSI, which relies on the processed low-cost data, to CWSI score, which relies on the measurements taken by the FLIR A655Sc, shows only a minor difference of only 1.42% for SR×2 and 1.86% for SR×4.
For more results, see Oz *et al.* (2025).

Low-cost thermal cameras are sensitive to radiation emitted from objects with temperatures in the range of 300 K. The native camera response is in grey level, which can be tied to object temperature but requires calibration. The camera suffers from two main drawbacks: ambient temperature-dependent non-uniformity response and low spatial resolution. Previous studies have tackled these drawbacks separately; notable are Kim *et al.* (2016) in SR, and Nugent *et al.* (2013) in NUC. An extensive account of related work can be found in Oz *et al.* (2025). This work presents progress over previous work by an end-to-end approach.

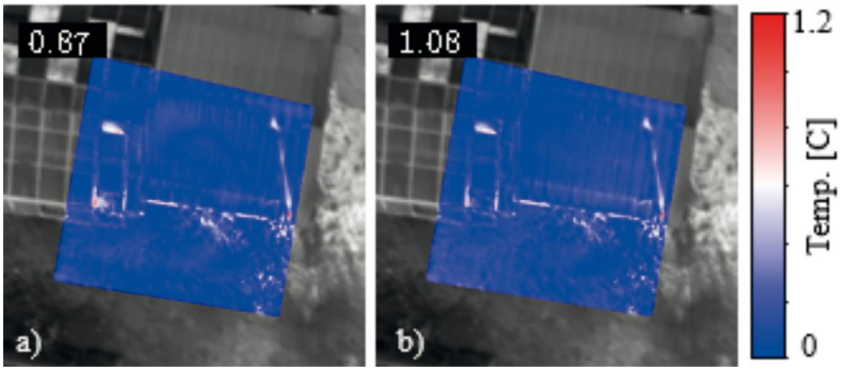

Figure 6. Results of the proposed end-to-end pipeline on real data with single image super-resolution: (a) NUC with SR×2. (b) NUC with SR×4. Adapted from Oz *et al.* (2025). The field of view is 15.6 m×15.6 m.

Conclusions

Partial results have shown that convolutional neural network architecture can provide machine learning algorithms that, upon training, can correct the uniformity, improve the spatial resolution, and estimate temperature with high accuracy with MAE close to 0.5 ^{0}C. In addition, results showed that this data can, in principle, be used further to estimate plant water status through CWSI calculations with an accuracy of better than 2%. Thus, learning algorithms supported by the camera models could compensate for the drawbacks of low-cost thermal cameras, potentially replacing costly scientific-grade radiometric cameras in remote sensing temperature monitoring and assessing the water status of crops in agricultural fields.

Acknowledgements

The authors thank Dr. Eitan Goldstein, Ohaliav Keisar, Moti Barak, Lavi Rosenfeld and Liad Reshef for data and engineering support and the Israeli Ministry of Agriculture for funding grant no. 20-12-0030.

References

Bahat, I., Netzer, Y., Grünzweig, J.M., Alchanatis, V., Peeters, A., Goldshtein, E., Ohana-Levi, N., Ben-Gal, A., & Cohen, Y. (2021). In-season interactions between vine vigor, water status, and wine quality in terrain-based management zones in a 'cabernet sauvignon' vineyard. Remote Sensing, 13, 1636. https://doi.org/10.3390/rs13091636

Berni, J., Zarco-Tejada, P., Sepulcre-Cantó, G., Fereres, E., & Villalobos, F. (2009). Mapping canopy conductance and cwsi in olive orchards using high resolution thermal remote sensing imagery. Remote Sensing of Environment, 113, 2380–2388.

Das, S., Christopher, J., Apan, A.A., Choudhury, M.R., Chapman, S.C., Menzies, N.W., & Dang, Y.P. (2020). UAV-thermal imaging: a robust technology to evaluate in-field crop water stress and yield variation of wheat genotypes. IEEE, India Geoscience and Remote Sensing Symposium (InGARSS), pp 138–141.

Katz, L., Ben-Gal, A., Litaor, M.I., Naor, A., Peres, M., Peeters, A., Alchanatis, V., & Cohen, Y. (2022). A spatiotemporal decision support protocol based on thermal imagery for variable rate drip irrigation of a peach orchard. Irrigation Science, 41, 215–233.

Kim, J., Lee, J.K., & Lee, K.M. (2016). Accurate image super-resolution using very deep convolutional networks. In The IEEE Conference on Computer Vision and Pattern Recognition (CVPR), Las Vegas, NV, USA, pp. 1646–1654. doi: 10.1109/CVPR.2016.182.

Klapp, I., Papini, S., & Sochen, N. (2017). Radiometric imaging by double exposure and gain calibration. Applied Optics, 56(20), 5639–5647.

Klapp, I., Yafin, P., Oz, N., Brand, O., Bahat, I., Goldshtein, E., Cohen, Y., Alchanatis, V., & Sochen, N. (2021). Computational end-to-end and super-resolution methods to improve thermal infrared remote sensing for agriculture. Precision Agriculture, 22, 452–474.

Mahlein, A.K. (2016). Plant disease detection by imaging sensors - parallels and specific demands for precision agriculture and plant phenotyping. Plant Disease, 100, 241–251.

Nugent, P.W., Shaw, J.A., & Pust, N.J. (2013). Correcting for focal-plane-array temperature dependence in microbolometer infrared cameras lacking thermal stabilization. Optical Engineering, 52, 061304.

Oz, N., Sochen, N., Markovich, O., Halamish, Z., Shpialter-Karol, L., & Klapp, I. (2020). Rapid super resolution for infrared imagery. Optics Express, 28, 27196–27209.

Oz, N., Sochen, N., Mendlovic, D., & Klapp, I. (2024a). Estimating temperatures with low-cost infrared cameras using physically-constrained deep neural networks. Optics Express, 32, 30565–30582.

Oz, N., Berman, O., Sochen, N., Mendlovic, D., & Klapp, I. (2024b). Simultaneous temperature estimation and nonuniformity correction from multiple frames. IEEE Transactions on Image Processing, 33, 5246–5259.

Oz, N., Sochen, N., Mendlovic, D., & Klapp, I. (2025). End-to-end pipeline for simultaneous temperature estimation and super resolution of low-cost uncooled infrared camera frames for precision agriculture applications. Non-peer reviewed preprint at arXiv: 2502.13985.

Ronneberger, O., Fischer, P., & Brox, P. (2015). U-net: Convolutional networks for biomedical image segmentation. In N. Navab, J. Hornegger, W. Wells, 7 A. Frangi (eds) Medical Image Computing and Computer-Assisted Intervention MICCAI 2015. Springer, Cham, pp. 234–241. https://doi.org/10.1007/978-3-319-24574-4_28